ACS APPLIED MATERIALS & INTERFACES

Research Article

www.acsami.org

Antimony-Doped Tin Oxide Nanorods as a Transparent Conducting Electrode for Enhancing Photoelectrochemical Oxidation of Water by Hematite

Yiqing Sun,[†,‡] William D. Chemelewski,[†] Sean P. Berglund,[†] Chun Li,[‡] Huichao He,[†] Gaoquan Shi,*[,‡] and C. Buddie Mullins*[,†]

[†]Departments of Chemical Engineering and Chemistry, Center for Electrochemistry, Texas Materials Institute, Center for Nano and Molecular Science, University of Texas at Austin, 1 University Station C0400, Austin, Texas 78712, United States

[‡]Department of Chemistry, Tsinghua University, Beijing 100084, People's Republic of China

Supporting Information

ABSTRACT: We report the growth of well-defined antimony-doped tin oxide (ATO) nanorods as a conductive scaffold to improve hematite's photoelectrochemical water oxidation performance. The hematite grown on ATO exhibits greatly improved performance for photoelectrochemical water oxidation compared to hematite grown on flat fluorine-doped tin oxide (FTO). The optimized photocurrent density of hematite on ATO is 0.67 mA/cm^2 (0.6 V vs Ag/AgCl), which is much larger than the photocurrent density of hematite on flat FTO (0.03 mA/cm^2). Using H_2O_2 as a hole scavenger, it is shown that the ATO nanorods indeed act as a useful scaffold and enhanced the bulk charge separation efficiency of hematite from 2.5% to 18% at 0.4 V vs Ag/AgCl.

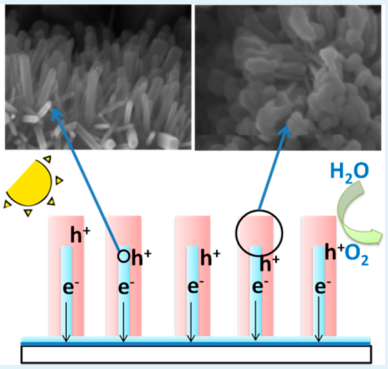

KEYWORDS: *nanorod scaffold, Fe_2O_3, water splitting, water oxidation, PEC, photoelectrochemistry*

INTRODUCTION

The photoelectrochemical (PEC) cell is one of the most promising devices to convert solar energy into hydrogen via water splitting.[1−4] Since the first reports of photoelectrodes for water splitting,[5,6] a variety of semiconductors have been explored for this purpose. TiO_2 has been extensively studied as a photoelectrode for water oxidation because of its low price, low environmental impact, and chemical stability.[7] However, TiO_2 has a large band gap (3.2 eV) and can only absorb a tiny fraction of the solar spectrum.[8] Some visible light photocatalysts, such as CdS, CdSe, and Cu_2O, are unstable, mainly due to photocorrosion in water under illumination.[9] However, some metal oxides show appropriate band gaps and reasonable stability; this list includes hematite (Fe_2O_3),[10,11] WO_3,[12,13] and $BiVO_4$.[14] Hematite, with a band gap of 2.1 eV, can absorb about 20% of the solar photon flux.[15] Furthermore, it is cheap and photoelectrochemically stable. Thus, hematite has been widely studied as a model semiconductor for PEC water oxidation.[16,17] Unfortunately, hematite's short hole diffusion length (<10 nm)[18] and low rate constant for water oxidation[19] severely limit its PEC performance.

A short charge diffusion length is a common problem for many metal oxide photocatalysts. Loading semiconductors on 3D conductive scaffolds is one strategy to address this issue.[20,21] Ideal 3D conductive scaffolds should have enough porous volume to load an amount of semiconductor capable of absorbing most of the incident light. Additionally, the scaffolds need to provide short conductive paths and be inexpensively fabricated. Previously, semiconducting catalysts have been loaded on Si nanowires,[22−24] $TiSi_2$ nanonets,[17,25,26] and carbon fibers.[27] Recently, several transparent conducting oxide scaffolds have also been reported, and they showed attractive properties. Grätzel et al. synthesized a 3D porous conducting oxide electrode by depositing a layer of niobium (Nb)-doped SnO_2 on porous TiO_2 using atomic layer deposition (ALD).[20] ALD has also been utilized for the fabrication of transparent conducting scaffolds by coating silica-based inverse opal frameworks with indium tin oxide (ITO) or Sb-doped tin oxide.[28,29] Unfortunately, ALD requires complicated and expensive equipment. A less costly synthesis technique is producing films from colloidal particles.[21] However, these porous films have less well-defined conduction pathways. Effective charge transport through electrodes is determined not only by the electrical conductivity of the scaffold but also by the transport path.[21] One-dimensional (1D) nanostructures could enhance charge collection by transporting charges through ordered, direct channels, thereby reducing the number of dead-ends.[30] Furthermore, 1D nanostructured materials tend

Received: December 6, 2013
Accepted: March 25, 2014
Published: March 26, 2014

   dx.doi.org/10.1021/am405628r | ACS Appl. Mater. Interfaces 2014, 6, 5494−5499

to have fewer grain boundaries.[31,32] Thus, it is possible that 1D nanostructures could increase the transport efficiency of many PEC materials.

In this report, we first synthesize well-defined antimony-doped tin oxide (ATO) nanorods on FTO using hydrothermal methods. Hematite was then electrochemically deposited on ATO nanorods and used as a model semiconductor for photoelectrochemical water oxidation. The scaffold supported hematite exhibited greatly improved performance for PEC water oxidation compared to hematite on FTO. Using H_2O_2 as a hole scavenger, we conclusively show that the transparent scaffold acts by enhancing the charge separation efficiency.

EXPERIMENTAL METHODS

Materials. Tin(IV) chloride hydrate (98%, Alfa Aesar), hydrochloric acid (ACS Reagent grade 36.5−38%), FTO coated glass substrates (1.5 cm × 1.5 cm, Pilkington, TEC15), iron(II) chloride (99%, anhydrous, Acros), ethanol (ACS grade, 200 proof, Pharmco-Aaper), and 1-methylimidazole (99%, Acros Organics) were used as received.

Synthesis of Sb-Doped SnO_2 Nanorods. FTO coated glass substrates were cleaned by alternate sonication in ethanol and deionized water for a total of 30 min. Then, the FTO substrates were seeded in 50 mL of 5 mM $SnCl_4$ solution (water:ethanol = 1:1) overnight and annealed at 550 °C for 30 min. Three pieces of seeded FTO were placed on the bottom of a Teflon-lined autoclave (125 mL, Parr Instrument Co.) containing a mixture of 25 mL of H_2O, 25 mL of ethanol, 2 mL of HCl, and 45 mg of $SnCl_4{\cdot}xH_2O$. To this solution were added varying amounts of 100 mM $SbCl_3$ ethanol solution, and the mixture was then sonicated for 15 min: 33, 67, 104, or 142 μL, corresponding to a 2.5, 5, 7.5, or 10% Sb/(Sn + Sb) atomic ratio. The hydrothermal reaction was performed at 200 °C for 12 h. After hydrothermal reaction, the films were annealed at 550 °C for 30 min. The corresponding Sb-doped ATO nanorods scaffolds were labeled as 2.5%-ATO, 5%-ATO, 7.5%-ATO, and 10%-ATO, respectively. Undoped SnO_2 nanorods were synthesized with the same procedures described above, but without adding $SbCl_3$.

Fe_2O_3 Synthesis. As described previously,[33] 0.818 g of NaCl and 0.287g of 1-methylimidazole were dissolved in 35 mL of water to which 0.75 mL of 0.5 M $FeCl_2$ solution was added. The pH of the electrolyte was then adjusted to 8.0 with 2 M HCl. An ATO film with an area of 1.65 cm^2 was used as the working electrode. FeOOH was deposited at a potential of −0.2 V vs Ag/AgCl. The charge passed during electrodeposition was 12.5, 25, 50, 75, 100, or 125 mC, resulting in different thicknesses. After electrodeposition, the samples were annealed at 550 °C for 4 h. The samples are referred to as $Fe_2O_3(x)$-y-ATO, where x is the electrodeposited charge and y is the Sb/(Sb + Sn) fraction in solution. Hematite on flat FTO was synthesized by the same process and labeled as $Fe_2O_3(x)$-FTO.

Material Characterization. X-ray diffraction (XRD) patterns were recorded using a Rigaku Spider X-ray diffractometer with a Cu Kα X-ray source. Scanning electron microscopy (SEM) images were taken with a Zeiss Supra 40 VP SEM using a 5 kV accelerating voltage. A Cary 5000 UV−vis spectrophotometer was used to measure the UV−vis transmission spectra. X-ray photoelectron spectroscopy (XPS) measurements were taken by a Kratos Axis Ultra photoelectron spectrometer using monochromated Al Kα as the excitation source.

Electrochemical Characterization. Photoelectrochemical measurements were performed in 1 M KOH using platinum wire as the counter electrode and Ag/AgCl in saturated KCl as the reference electrode. The area of the films exposed to the electrolyte was 0.22 cm^2, set by a rubber O-ring. Illumination was through the FTO/film interface (often referred to as "backside") and the illumination area was masked such that the illuminated and solution exposed areas were the same. Backside illumination was chosen because, for a diverse subset of samples, backside photocurrents were higher than frontside photocurrents. For white light measurements, the light source was a 150 W xenon lamp (Newport, model 66452) with an AM1.5 filter (Newport, Schott KG3). The output power was measured with a thermopile detector (Newport) and adjusted to 100 mW/cm^2. For visible light measurements, an additional filter (Newport, cutoff filter, 420 nm) was added to the light source. All the electrochemical testing was performed with a CHI660D potentiostat. Incident photon-to-current conversion efficiencies (IPCE) were calculated from chronoamperometry measurements using a Newport Oriel Cornerstone 130 1/8 m monochromator. The monochromator slit size was set to 0.75 mm × 2 mm, and the light power was measured with a silicon photodetector (Newport, 818-UV). A representative incident light power density curve is shown in Figure S1 (Supporting Information). The IPCE values were calculated using the following equation

$$\mathrm{IPCE} = (1240 \times J)/(\lambda \times P)$$

where J is the measured photocurrent density (mA/cm^2) and P is the incident light power density (mW/cm^2) for each wavelength λ (nm).

RESULTS AND DISCUSSION

Figure 1 gives the top-view and cross-sectional scanning electron microscopy (SEM) images of 10%-ATO nanorods.

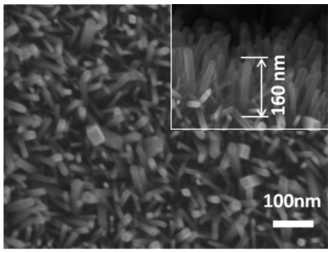

Figure 1. SEM image of 10%-ATO nanorod film. The inset is the SEM image of the same film on a 70° holder.

The diameter of the nanorods varies from 15 to 30 nm while their length is about 160 nm. The SEM images of undoped SnO_2, 1%-ATO, and 5%-ATO nanorods are shown in Figures S2−S4 (Supporting Information). There is little morphology difference between undoped SnO_2 and ATO nanorods with Sb content during growth of up to 10%. However, when the Sb fraction in the solution for hydrothermal reaction increased to 12.5%, no nanorods grew on the FTO substrate (Figure S5, Supporting Information).

The X-ray diffraction (XRD) patterns of undoped SnO_2 and ATO nanorods after annealing at 550 °C are shown in Figure 2a. The diffraction peaks of undoped SnO_2 nanorods can be indexed to tetragonal SnO_2.[34] ATO nanorods with different doping levels of Sb have XRD patterns similar to that of the undoped SnO_2 nanorods. This result implies that Sb is acting as a dopant and not segregating out as another phase. X-ray photoelectron spectroscopy (XPS) was used to determine the amount of Sb doping in the films. The XPS spectra of Sn and Sb are shown in Figure S6 (Supporting Information). The intensity of the Sb ($3d_{3/2}$) peaks increases monotonically with the Sb fraction in the hydrothermal reaction. The Sb content of the nanorods was evaluated by comparing the areas of the Sn ($3d_{3/2}$) and Sb ($3d_{3/2}$) peaks (Figure 2b), and Sb appears to easily incorporate into tin oxide. Light absorption measurements of the ATO as a function of doping are shown in Figure S7 (Supporting Information) and demonstrate that they are indeed highly transparent for all doping levels.

SEM images of hematite grown on the nanorods are shown in Figure 3. When the charge used for electrodeposition increased from 12.5 to 75mC, the diameters of the nanorods

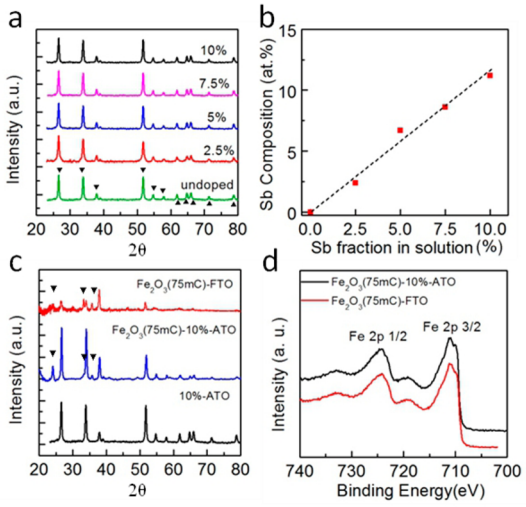

Figure 2. (a) XRD patterns of undoped SnO_2, 2.5%-ATO, 5%-ATO, 7.5%-ATO, and 10% ATO nanorods. (b) Sb fraction in the hydrothermal reactor during growth vs Sb fraction in the ATO nanorods as determined by XPS. (c) XRD patterns of Fe_2O_3 (75mC)-FTO, Fe_2O_3 (75mC)-10%-ATO, and bare 10%-ATO. The peaks marked by (▼) correspond to hematite. (d) XPS patterns of Fe (2p) region for Fe_2O_3 (75mC)-FTO and Fe_2O_3 (75mC)-10%-ATO.

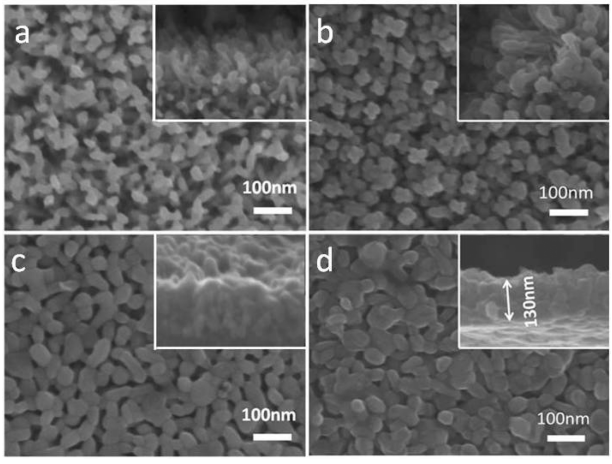

Figure 3. Top-view SEM images of (a) Fe_2O_3 (12.5mC)-10%-ATO, (b) Fe_2O_3 (75mC)-10%-ATO, (c) Fe_2O_3 (125mC)-10%-ATO, and (d) Fe_2O_3 (75mC)-FTO. For all images, the inset is the SEM of the same film on a 70° holder.

increased from ~20 to ~40 nm (Figure 3a,b), implying an Fe_2O_3 thickness of about 10 nm. As more hematite was added, it continued to fill the pores between the nanorods (Figure 3c). Figure 3d shows the top-view and cross-sectional SEM images of Fe_2O_3 (75mC)-FTO. The XRD patterns of hematite on flat FTO and ATO nanorods are shown in Figure 2c, with a higher resolution comparison of the hematite peaks in Figure S6 (Supporting Information), showing a slightly different texture depending on the substrate.[35] Such a small difference is expected to have a minimal impact on performance. The XPS spectra of the Fe (2p) region is shown in Figure 2d, with the shape matching that seen in the literature for hematite.[36] Measurements in the dark in the presence of the ferricyanide/ferrocyanide redox couple confirm that the Fe_2O_3 has few pinholes and forms an effective blocking layer on the ATO, evidencing its uniform coverage (Figure S8, Supporting Information).

The photocatalytic activity of the hematite on different scaffolds was characterized under backside illumination by AM 1.5G simulated sunlight (light intensity set to 100 mW cm^{-2}); backside illumination gave higher photocurrents for all the films for which frontside illumination was tested (Figure S9, Supporting Information). Figure 4a shows the photocurrent

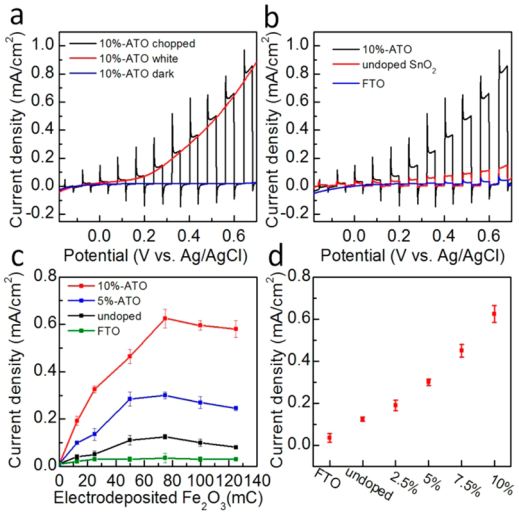

Figure 4. (a) Linear sweep voltammetry (LSV) scans of Fe_2O_3 (75mC)-10%-ATO films under irradiation (labeled "white"), chopped irradiation (labeled "chopped"), and without irradiation (labeled "dark"). (b) Chopped LSV scans of Fe_2O_3 (75mC)-FTO, Fe_2O_3 (75mC)-10%-ATO, and Fe_2O_3 (75mC)-undoped SnO_2. (c) Photocurrent densities obtained from the LSV scans of Fe_2O_3 (different quantities of electrodeposited charge) on various substrates at 0.6 V vs Ag/AgCl. (d) Photocurrent density at 0.6 V vs Ag/AgCl obtained from the LSV scans of 75 mC Fe_2O_3 on various substrates. All scans are done at 25 mV/s in 1 M KOH; illumination is simulated solar (AM1.5) with an intensity of 100 mW/cm^2.

density characteristic of Fe_2O_3(75mC)-10%-ATO in 1.0 M KOH. Without irradiation, no substantial current was observed before 0.7 V. In contrast, the photocurrent density was measured to be 0.67 mA/cm^2 at 0.6 V vs Ag/AgCl under illumination. The photocurrent densities of Fe_2O_3 (75mC)-FTO, Fe_2O_3 (75mC)-10%-ATO, and Fe_2O_3 (75mC)-undoped SnO_2 under chopped light are shown in Figure 4b. At 0.6 V vs Ag/AgCl, the photocurrent density of Fe_2O_3 (75mC)-FTO is 0.03 mA/cm^2, whereas the photocurrent density of Fe_2O_3(75mC)-undoped SnO_2 is only 0.11 mA/cm^2, both being significantly lower than that of Fe_2O_3 (75mC)-10%-ATO films. We note that the photocurrents measured for the hematite grown on FTO are quite low compared to other reports using different synthesis techniques, although they are similar to reports of hematite grown by annealing of electrodeposited iron precursors.[37]

The photocurrent densities obtained from the LSV scans of different thicknesses of Fe_2O_3 on FTO, undoped SnO_2 nanorods, 5%-ATO, and 10%-ATO nanorods at 0.6 V vs Ag/AgCl are shown in Figure 4c. As the thickness of Fe_2O_3 increases from 12.5 to 75 mC, photocurrent densities for 10%-ATO nanorod scaffolds increase to a maximum value and then slightly decrease for thicker hematite layers (greater than 75 mC). This phenomenon was also observed for 5%-ATO and

dx.doi.org/10.1021/am405628r | ACS Appl. Mater. Interfaces 2014, 6, 5494−5499

undoped SnO_2 nanorod scaffolds. Meanwhile, for the same quantity of electrodeposited hematite, photocurrent densities on undoped SnO_2 nanorods are higher than that on flat FTO but lower than that on doped SnO_2 films. Photocurrent densities of hematite (75mC) on different scaffolds at 0.6 V vs Ag/AgCl are shown in Figure 4d. It is found that the photoactivity of hematite (75mC) on different scaffolds increases according to the following trend: FTO < undoped SnO_2 < 2.5%-ATO < 5%-ATO < 7.5%-ATO < 10%-ATO. This is consistent with previous reports that the conductivity of Sb-doped SnO_2 films increases as the Sb composition in the film increases.[38−40] Therefore, the increase in photocurrent with increasing Sb content is likely due to higher nanorod conductivity.

Chronoamperometry was used to further characterize the stability of hematite on different scaffolds. Amperometric $i-t$ curves measured in 1 M KOH solution at a constant applied potential of 0.6 V vs Ag/AgCl are shown in Figure S10 (Supporting Information). After 1500 s, the photocurrent density of Fe_2O_3(75mC)-10%-ATO and Fe_2O_3(75mC)-FTO drops from 0.67 and 0.06 mA/cm^2 to 0.52 and 0.048 mA/cm^2, respectively. The fast decease in the first few seconds is caused by photocurrent transients upon turning on the light. The photocurrent transient is due to the accumulation of the holes at the electrode/electrolyte interface without injection to the electrolyte.[41,42] The fact that both films show a photocurrent decrease of 20% indicates that the scaffolds have little impact on the stability of hematite.

UV−vis absorption data for Fe_2O_3(75mC)-FTO and Fe_2O_3(75mC)-10%-ATO are shown in Figure S11 (Supporting Information). Hematite exhibits broad absorption above about 600 nm, consistent with a band gap of 2.1 eV. Figure 5a gives the incident photon-to-current efficiency spectra (IPCE) of Fe_2O_3(75mC)-FTO and Fe_2O_3(75mC)-10%-ATO (Figure S12, Supporting Information shows the APCE of the same samples). The hematite on 10%-ATO has an IPCE of about 20% at short wavelengths, whereas the IPCE of hematite on FTO only reaches 4.8% at the same wavelength. We also

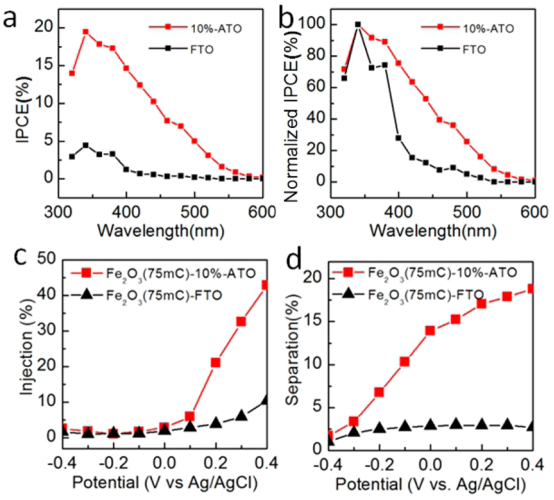

Figure 5. (a) IPCE of Fe_2O_3(75mC)-FTO and Fe_2O_3(75)-10%-ATO. The test was run at 0.6 V vs Ag/AgCl in 1 M KOH. (b) Normalized IPCE curves of films shown in (a). (c) Charge injection yield for Fe_2O_3(75mC)-FTO and Fe_2O_3(75mC)-10%-ATO electrodes in the 1 M KOH electrolyte. (d) Charge separation yield in Fe_2O_3(75mC)-FTO and Fe_2O_3(75mC)-10%-ATO electrodes.

normalized the IPCE of the films to look for any relative shape differences (Figure 5b). This clearly shows that the IPCE is enhanced at longer wavelengths for hematite on conductive nanorods. This implies that the ATO nanorod is indeed improving charge collection for photons that penetrate deeper into the hematite film.

To further verify the mechanism by which the ATO nanorods improve the PEC activity of Fe_2O_3, H_2O_2 was used as a hole scavenger to separate the performance increase attributable to charge separation in Fe_2O_3 (the charge extraction yield in the limit of perfect catalytic activity) versus charge injection (or charge transfer kinetics).[42,43] Chopped light chronoamperometry curves of Fe_2O_3(75mC)-10%-ATO and Fe_2O_3(75mC)-FTO were measured separately in 1 M KOH and a mixture of 0.5 M H_2O_2 and 1 M KOH (Figure S13, Supporting Information). In the measurements without H_2O_2, there are transient photocurrents at all potentials. These transients are usually caused by hole accumulation at the electrode/electrolyte interface. The positive photocurrent transient observed upon illumination is due to the accumulation of the holes at the electrode/electrolyte interface without injection to the electrolyte, whereas the negative current transient upon light blocking is because of the back reaction of electrons from the conduction band with the accumulated holes.[44] In contrast, when the films are measured with H_2O_2, Faradaic photocurrents without transients are observed at all potentials. This verifies that addition of H_2O_2 removes the injection barrier at the electrode/electrolyte interface and nearly all the holes that reach the interface are injected to the electrolyte.

The total photocurrent generated by the film in 1 M KOH can be expressed as[42]

$$J^{H_2O}{}_{photocurrent} = J_{absorbed} \times P_{charge\ separation} \times P_{charge\ injection}$$

where $J^{H_2O}{}_{photocurrent}$ represents the steady-state water oxidation photocurrent density at a set potential, $J_{absorbed}$ is the photocurrent calculated from the absorption spectra with the small amount of FTO and ATO absorption subtracted before calculating $J_{absorbed}$, $P_{charge\ separation}$ is the fraction of the photogenerated holes that reach the electrode/electrolyte interface, and $P_{charge\ injection}$ is the fraction of holes that make it to the interface that are injected to the solution.

For the H_2O_2 oxidation over hematite, $P_{charge\ injection}$ is approximately 100% at all potentials tested. Thus, the above formula simplifies to

$$J^{H_2O_2}{}_{photocurrent} = J_{absorbed} \times P_{charge\ separation}$$

The values of the $J^{H_2O}{}_{photocurrent}$ and $J^{H_2O_2}{}_{photocurrent}$ are shown in Figure S13 (Supporting Information). $J_{absorbed}$ of Fe_2O_3 (75mC)-FTO and Fe_2O_3 (75mC)-10%-ATO was calculated to be 8.8 and 5.6 mA/cm^2 with cutoff wavelengths for the integration set to 350 and 580 nm. With the values of the $J^{H_2O_2}{}_{photocurrent}$, $J_{absorbed}$, and $J^{H_2O}{}_{photocurrent}$ determined, the charge separation yield $P_{charge\ separation}$ can be calculated using $J^{H_2O_2}{}_{photocurrent}/J_{absorbed}$. The charge injection yield $P_{charge\ injection}$ can be found using $J^{H_2O}{}_{photocurrent}/J^{H_2O_2}{}_{photocurrent}$. The charge injection and charge separation yields at different potentials are given in Figure 5c,d. For both films, the injection yield of the hematite is near zero before 0 V vs Ag/AgCl and then the injection increases to 45% and 11% at 0.4 V vs Ag/AgCl for Fe_2O_3 (75mC)-10%-ATO and Fe_2O_3 (75mC)-FTO, respectively. Charge separation efficiency begins to rise at −0.4 V vs

dx.doi.org/10.1021/am405628r | ACS Appl. Mater. Interfaces 2014, 6, 5494−5499

Ag/AgCl and reaches 18% for Fe_2O_3 (75mC)-10%-ATO versus 2.5% for Fe_2O_3 (75mC)-FTO at 0.4 V vs Ag/AgCl. This directly shows that the ATO scaffold enhances charge separation, particularly at lower potentials; however, the efficiency remains below what is needed for a practical device.

Above 0.1 V vs Ag/AgCl, the Fe_2O_3 (75mC)-10%-ATO films show significantly enhanced charge injection efficiency. This could be caused by an increase in the hole flux per unit area. If the recombination rate due to surface states is near saturation for Fe_2O_3-FTO films, and given that the hematite surface area of Fe_2O_3-10%-ATO films is about 5 times higher than that of Fe_2O_3-FTO films (Figures S14 and S15, Supporting Information) while the hole flux is also about 5 times higher for potentials beyond 0.1 V, the additional hole flux beyond the surface state current saturation is then free to be injected to the solution. Alternatively, the improved injection could be due to thinner hematite layers on the SnO_2 nanorods compared to that on flat FTO as the thinner layers would become fully depleted at lower potentials. Beyond full depletion, any increase in potential pulls down the valence band and increases the oxidation power of the holes that arrive at the interface. Our results do not allow us to differentiate between these two possibilities.

CONCLUSIONS

A series of well-defined ATO nanorod films have been synthesized hydrothermally. Hematite was grown on SnO_2 conducting scaffolds with varying amounts of Sb and on commercial, flat FTO. A photocurrent density of 0.67 mA/cm^2 at 0.6 V vs Ag/AgCl was obtained with a 10%-ATO scaffold, which is much larger than the comparable photocurrent density for hematite loaded on commercial FTO (about 0.03 mA/cm^2). We also found that, for the same quantity of electrodeposited hematite, the PEC water splitting performance on different scaffolds was 10%-ATO > 7.5%-ATO > 5%-ATO > 2.5%-ATO > undoped SnO_2 nanorod > FTO. Given that the ATO nanorod films have the same structure as the undoped SnO_2 nanorods and that the hematite is consistently grown, we conclude that higher Sb content ATO films have higher performance due to improved scaffold conductivity. H_2O_2 was used as a hole scavenger to further study the performance increase of Fe_2O_3 on ATO scaffolds. It was found that the charge separation efficiency as well as the charge injection efficiency is enhanced using ATO scaffolds. However, at lower potentials more useful for practical application, the majority of the increase is due to improved charge separation.

ASSOCIATED CONTENT

Supporting Information

Included are the experimental methods, SEM images of ATO nanorods, XPS spectra of Sn and Sb ($3d_{3/2}$) regions, amperometric *i*−*t* stability testing plots, UV−vis absorbance, raw hole scavenger *i*−*t* data, and CV measurements. This material is available free of charge via the Internet at http://pubs.acs.org.

AUTHOR INFORMATION

Corresponding Authors

*E-mail: mullins@che.utexas.edu (C.B.M.).
*E-mail: gshi@tsinghua.edu.cn (G.S.).

Notes

The authors declare no competing financial interest.

ACKNOWLEDGMENTS

The authors gratefully acknowledge the Division of Chemical Sciences, Geosciences, and Biosciences, Office of Basic Energy Sciences of the U.S. Department of Energy through Grant DEFG02-09ER16119, and the Welch Foundation (Grant F-1436) for funding this work. Additionally, we acknowledge the National Science Foundation for a Grant (no. 0618242) that funded the X-ray photoelectron spectrometer used for these studies. Y.S. thanks the China Scholarship Council for financial support. W.D.C. thanks the National Science Foundation Graduate Research Fellowship Program for support of this work (Grant DGE-1110007 AMD 004).

REFERENCES

(1) Bard, A. J.; Fox, M. A. Artificial Photosynthesis: Solar Splitting of Water to Hydrogen and Oxygen. *Acc. Chem. Res.* **1995**, *28*, 141−145.
(2) Gratzel, M. Photoelectrochemical Cells. *Nature* **2001**, *414*, 338−344.
(3) Walter, M. G.; Warren, E. L.; McKone, J. R.; Boettcher, S. W.; Mi, Q.; Santori, E. A.; Lewis, N. S. Solar Water Splitting Cells. *Chem. Rev.* **2010**, *110*, 6446−6473.
(4) Chen, X.; Shen, S.; Guo, L.; Mao, S. S. Semiconductor-Based Photocatalytic Hydrogen Generation. *Chem. Rev.* **2010**, *110*, 6503−6570.
(5) Boddy, P. J. Oxygen Evolution on Semiconducting TiO_2. *J. Electrochem. Soc.* **1968**, *115*, 199−203.
(6) Fujishima, A.; Honda, K. Electrochemical Photolysis of Water at a Semiconductor Electrode. *Nature* **1972**, *238*, 37−38.
(7) Hernandez-Alonso, M. D.; Fresno, F.; Suarez, S.; Coronado, J. M. Development of Alternative Photocatalysts to TiO_2: Challenges and Opportunities. *Energy Environ. Sci.* **2009**, *2*, 1231−1257.
(8) Bak, T.; Nowotny, J.; Rekas, M.; Sorrell, C. C. Photo-electrochemical Hydrogen Generation from Water Using Solar Energy. Materials-Related Aspects. *Int. J. Hydrogen Energy* **2002**, *27*, 991−1022.
(9) Hong, S. J.; Lee, S.; Jang, J. S.; Lee, J. S. Heterojunction $BiVO_4$/WO_3 Electrodes for Enhanced Photoactivity of Water Oxidation. *Energy Environ. Sci.* **2011**, *4*, 1781−1787.
(10) Kay, A.; Cesar, I.; Graetzel, M. New Benchmark for Water Photooxidation by Nanostructured α-Fe_2O_3 Films. *J. Am. Chem. Soc.* **2006**, *128*, 15714−15721.
(11) Sivula, K.; Le Formal, F.; Graetzel, M. Solar Water Splitting: Progress Using Hematite (α-Fe_2O_3) Photoelectrodes. *ChemSusChem* **2011**, *4*, 432−449.
(12) Kim, J. K.; Shin, K.; Cho, S. M.; Lee, T.-W.; Park, J. H. Synthesis of Transparent Mesoporous Tungsten Trioxide Films with Enhanced Photoelectrochemical Response: Application to Unassisted Solar Water Splitting. *Energy Environ. Sci.* **2011**, *4*, 1465−1470.
(13) He, H.; Berglund, S. P.; Xiao, P.; Chemelewski, W. D.; Zhang, Y.; Mullins, C. B. Nanostructured Bi_2S_3/WO_3 Heterojunction Films Exhibiting Enhanced Photoelectrochemical Performance. *J. Mater. Chem. A* **2013**, *1*, 12826−12834.
(14) Walsh, A.; Yan, Y.; Huda, M. N.; Al-Jassim, M. M.; Wei, S. H. Band Edge Electronic Structure of BiVO4: Elucidating the Role of the Bi s and V d Orbitals. *Chem. Mater.* **2009**, *21*, 547−551.
(15) Wheeler, D. A.; Wang, G.; Ling, Y.; Li, Y.; Zhang, J. Z. Nanostructured Hematite: Synthesis, Characterization, Charge Carrier Dynamics, and Photoelectrochemical Properties. *Energy Environ. Sci.* **2012**, *5*, 6682−6702.
(16) Brillet, J.; Gratzel, M.; Sivula, K. Decoupling Feature Size and Functionality in Solution-Processed, Porous Hematite Electrodes for Solar Water Splitting. *Nano Lett.* **2010**, *10*, 4155−4160.
(17) Lin, Y.; Zhou, S.; Sheehan, S. W.; Wang, D. Nanonet-Based Hematite Heteronanostructures for Efficient Solar Water Splitting. *J. Am. Chem. Soc.* **2011**, *133*, 2398−2401.

(18) Bjorksten, U.; Moser, J.; Gratzel, M. Photoelectrochemical Studies on Nanocrystalline Hematite Films. *Chem. Mater.* **1994**, *6*, 858−863.
(19) Dareedwards, M. P.; Goodenough, J. B.; Hamnett, A.; Trevellick, P. R. Electrochemistry and Photoelectrochemistry of Iron(III) Oxide. *J. Chem. Soc., Faraday Trans. I* **1983**, *79*, 2027−2041.
(20) Stefik, M.; Cornuz, M.; Mathews, N.; Hisatomi, T.; Mhaisalkar, S.; Gräetzel, M. Transparent, Conducting Nb:SnO_2 for Host−Guest Photoelectrochemistry. *Nano Lett.* **2012**, *12*, 5431−5435.
(21) Peng, Q.; Kalanyan, B.; Hoertz, P. G.; Miller, A.; Kim, D. H.; Hanson, K.; Alibabaei, L.; Liu, J.; Meyer, T. J.; Parsons, G. N.; Glass, J. T. Solution-Processed, Antimony-Doped Tin Oxide Colloid Films Enable High-Performance TiO_2 Photoanodes for Water Splitting. *Nano Lett.* **2013**, *13*, 1481−1488.
(22) Mayer, M. T.; Du, C.; Wang, D. Hematite/Si Nanowire Dual-Absorber System for Photoelectrochemical Water Splitting at Low Applied Potentials. *J. Am. Chem. Soc.* **2012**, *134*, 12406−12409.
(23) Shi, J.; Hara, Y.; Sun, C.; Anderson, M. A.; Wang, X. Three-Dimensional High-Density Hierarchical Nanowire Architecture for High-Performance Photoelectrochemical Electrodes. *Nano Lett.* **2011**, *11*, 3413−3419.
(24) Shi, J.; Wang, X. Hierarchical TiO_2−Si Nanowire Architecture with Photoelectrochemical Activity under Visible Light Illumination. *Energy Environ. Sci.* **2012**, *5*, 7918−7922.
(25) Banerjee, S.; Mohapatra, S. K.; Misra, M. Water Photooxidation by $TiSi_2$−TiO_2 Nanotubes. *J. Phys. Chem. C* **2011**, *115*, 12643−12649.
(26) Lin, Y.; Zhou, S.; Liu, X.; Sheehan, S.; Wang, D. TiO_2/$TiSi_2$ Heterostructures for High-Efficiency Photoelectrochemical H_2O Splitting. *J. Am. Chem. Soc.* **2009**, *131*, 2772−2773.
(27) Zhao, W.; Bai, Z.; Ren, A.; Guo, B.; Wu, C. Sunlight Photocatalytic Activity of CdS Modified TiO_2 Loaded on Activated Carbon Fibers. *Appl. Surf. Sci.* **2010**, *256*, 3493−3498.
(28) Riha, S. C.; Vermeer, M. J. D.; Pellin, M. J.; Hupp, J. T.; Martinson, A. B. F. Hematite-Based Photo-oxidation of Water Using Transparent Distributed Current Collectors. *ACS Appl. Mater. Interfaces* **2013**, *5*, 360−367.
(29) Moir, J.; Soheilnia, N.; O'Brien, P.; Jelle, A.; Grozea, C. M.; Faulkner, D.; Helander, M. G.; Ozin, G. A. Enhanced Hematite Water Electrolysis Using a 3D Antimony-Doped Tin Oxide Electrode. *ACS Nano* **2013**, *7*, 4261−4274.
(30) Hochbaum, A. I.; Yang, P. Semiconductor Nanowires for Energy Conversion. *Chem. Rev.* **2010**, *110*, 527−546.
(31) Krishnamoorthy, T.; Tang, M. Z.; Verma, A.; Nair, A. S.; Pliszka, D.; Mhaisalkar, S. G.; Ramakrishna, S. A Facile Route to Vertically Aligned Electrospun SnO_2 Nanowires on a Transparent Conducting Oxide Substrate for Dye-Sensitized Solar Cells. *J. Mater. Chem.* **2012**, *22*, 2166−2172.
(32) Zhu, K.; Neale, N. R.; Miedaner, A.; Frank, A. J. Enhanced Charge-Collection Efficiencies and Light Scattering in Dye-Sensitized Solar Cells Using Oriented TiO_2 Nanotubes Arrays. *Nano Lett.* **2007**, *7*, 69−74.
(33) Chemelewski, W. D.; Lee, H.; Lin, J.; Bard, A. J.; Mullins, C. B. Amorphous FeOOH Oxygen Evolution Reaction Catalyst for Photoelectrochemical Water Splitting. *J. Am. Chem. Soc.* **2014**, *136*, 2843−2850.
(34) Mallesham, B.; Sudarsanam, P.; Raju, G.; Reddy, B. M. Design of Highly Efficient Mo And W-Promoted SnO_2 Solid Acids for Heterogeneous Catalysis: Acetalization of Bio-Glycerol. *Green Chem.* **2013**, *15*, 478−489.
(35) Chaudhari, N. K.; Kim, H. C.; Son, D.; Yu, J. S. Easy Synthesis and Characterization of Single-Crystalline Hexagonal Prism-Shaped Hematite α-Fe_2O_3 in Aqueous Media. *CrystEngComm* **2009**, *11*, 2264−2267.
(36) Baltrusaitis, J.; Cwiertny, D. M.; Grassian, V. H. Adsorption of Sulfur Dioxide on Hematite and Goethite Particle Surfaces. *Phys. Chem. Chem. Phys.* **2007**, *9*, 5542−5554.
(37) Spray, R. L.; Choi, K. S. Photoactivity of Transparent Nanocrystalline Fe_2O_3 Electrodes Prepared via Anodic Electrodeposition. *Chem. Mater.* **2009**, *21*, 3701−3709.
(38) Mazloom, J.; Ghodsi, F. E.; Gholami, M. Fiber-like Stripe ATO (SnO_2:Sb) Nanostructured Thin Films Grown by Sol-Gel Method: Optical, Topographical and Electrical Properties. *J. Alloys Compd.* **2013**, *579*, 384−393.
(39) Terrier, C.; Chatelon, J. P.; Berjoan, R.; Roger, J. A. Sb-Doped SnO_2 Transparent Conducting Oxide from the Sol-Gel Dip-Coating Technique. *Thin Solid Films* **1995**, *263*, 37−41.
(40) Terrier, C.; Chatelon, J. P.; Roger, J. A. Electrical and Optical Properties of Sb:SnO_2 Thin Films Obtained by the Sol-Gel Method. *Thin Solid Films* **1997**, *295*, 95−100.
(41) Itoh, K.; Bockris, J. O. Thin Film Photoelectrochemistry Iron Oxide. *J. Electrochem. Soc.* **1984**, *131*, 1266−1271.
(42) Dotan, H.; Sivula, K.; Graetzel, M.; Rothschild, A.; Warren, S. C. Probing the Photoelectrochemical Properties of Hematite (α-Fe_2O_3) Electrodes Using Hydrogen Peroxide as a Hole Scavenger. *Energy Environ. Sci.* **2011**, *4*, 958−964.
(43) Chemelewski, W. D.; Hahn, N. T.; Mullins, C. B. Effect of Si Doping and Porosity on Hematite's (α-Fe_2O_3) Photoelectrochemical Water Oxidation Performance. *J. Phys. Chem. C* **2012**, *116*, 5255−5261.
(44) Iwanski, P.; Curran, J. S.; Gissler, W.; Memming, R. The Photoelectrochemical Behavior Of Ferric-Oxide in the Presence of Redox Reagents. *J. Electrochem. Soc.* **1981**, *128*, 2128−2133.